Journal of Electron Spectroscopy and Related Phenomena 170 (2009) 49–56

Contents lists available at ScienceDirect

Journal of Electron Spectroscopy and Related Phenomena

journal homepage: www.elsevier.com/locate/elspec

Radiation sensitivity of natural organic matter: Clay mineral association effects in the Callovo-Oxfordian argillite

T. Schäfer[a,*], P. Michel[a], F. Claret[b], T. Beetz[c], S. Wirick[d], C. Jacobsen[d]

[a] Forschungszentrum Karlsruhe, Institut für Nukleare Entsorgung, PO Box 3640, 76021 Karlsruhe, Germany
[b] BRGM, Environment and Process Division 3, Avenue Claude Guillemin, F-45060 Orleans Cedex 2, France
[c] Xradia, Inc., 4075 Sprig Dr., Concord, CA 94520, USA
[d] State University of New York at Stony Brook, Department of Physics and Astronomy, Stony Brook, NY 11794, USA

ARTICLE INFO

Article history:
Available online 27 May 2008

Keywords:
XANES
STXM
NEXAFS
Radiation damage
Clay minerals
Callovo-Oxfordian

ABSTRACT

Clay-rich low-organic carbon formations (e.g., Callovo-Oxfordian argillite in France and Opalinus Clay in Switzerland) are considered as host rocks for radioactive waste disposal. The clay-organic carbon has a strong impact on the chemical stability of the clays. For this reason, the nature of the clay-organic carbon, the release of hydrophilic organic compounds, namely, humic (HA) and fulvic acids (FA) and the radiation sensitivity of the undisturbed host rock organics was investigated. The clay sample originates from Oxfordian argillite (447 m depth, borehole EST 104). HA and FA were extracted following the standard International Humic Substance Society (IHSS) isolation procedure. Synchrotron based (C-, K-, Ca-, O- and Fe-edge XANES) scanning transmission X-ray microscopy (STXM) and FT-IR microspectroscopy was used to identify under high spatial resolution the distribution of clay-organic matter with different functionality using principal component and cluster analysis. The results show that in this old (Jurassic) geological formation, small parts of the organic inventory (1–5%) keeps the structure/functionality and can be mobilized as hydrophilic humic substance type material (HA and FA). Target spectra analysis shows best correlation for isolated humic acids with organics found in smectite-rich regions, whereas the extractable FA has better spectral similarities with the illite mixed layer minerals (MLM) regions. After radiation of 1.7 GGy under helium atmosphere the same rock sample area was investigated for radiation damage. Radiation damage in the smectite and illite–MLM associated organic matter is comparably low with 20–30% total oxygen mass loss and 13–18% total carbon mass loss. A critical dose d_c of 2.5 GGy and a optical density after infinite radiation (OD_∞) of 54% was calculated under room temperature conditions. C(1s) XANES show a clear increase in C=C bonds especially in the illite–MLM associated organics. This results suggests a combination of the formation of C=C bond due to crosslinking via polymerization and mass loss due to bond breaking (scissioning) in the main chain or in side groups of the organic macromolecules upon irradiation.

1. Introduction

Clay-organic matter studies focus predominantly on the process of biogeochemical carbon cycling and the understanding of carbon degradation/prevention pathways in aquatic systems. About 90% of the preserved organic material (OM) in the global carbon cycle resides in amorphous, kerogen-type macromolecules disseminated in shale or other sedimentary rocks [1]. Over 90% of this total sedimentary organic matter cannot be physically separated from its mineral matrix. Several theories [2,3], namely, the classical degradation–recondensation pathway [4], the selective preservation [5], the natural sulphurization [6] and the sorptive protection pathway [7] have been proposed to explain this sedimentary organic matter preservation in marine environments. Residual organic matter in diagenetic overprinted shales or argillites of marine or terrestrial origin still show some extractable organic material, i.e., humic (HA) and/or fulvic acids (FA) [8–11].

The long-term deep geological disposal and biosphere isolation of high-level nuclear waste (HLW) is one of the current worldwide scientific challenges. Clay-rich low-organic carbon sediments are considered as possible host rock formations for deep geological disposal of nuclear waste. This poses the question, if mineral preserved mostly insoluble organic matter (bitumen and kerogen) can generate soluble compounds (HA and FA) having complexation properties with respect to radionuclides that might change the radionuclide transport mechanism (i.e., colloidal transport) [12–14]. Another aspect (not discussed in this paper) that has to

* Corresponding author. Tel.: +49 7247 82 5494; fax: +49 7247 82 3927.
E-mail address: schaefer@ine.fzk.de (T. Schäfer).

0368-2048/$ – see front matter © 2008 Elsevier B.V. All rights reserved.
doi:10.1016/j.elspec.2008.05.007

be considered with respect to the long-term evolution of different barriers in the multi-barrier concept of a repository is the change in chemical stability of backfill clay and/or host rock clay due to clay-organic association [15,10,16]. The emplacement of high-level waste (HLW) container will expose the multi-barrier system (e.g., backfill material) in addition to elevated radiation. The maximum absorbed gamma dose before the container fails (approx. 1000a) was calculated to be 0.7 MGy [17]. This gamma dose is significantly below the cumulative absorbed dose of 10 GGy expected in commercial high-level nuclear waste glass after 1000a storage time [18] and below the amorphization dose of approximately 30 GGy for the clay mineral montmorillonite [19]. Studies on gamma radiation sensitivity of thermally immature black shales have shown that kerogen is not affected by doses ranging from 1 to 9 MGy, whereas the amount of hydrophilic bitumen and high-molecular weight acyclic carboxylic acids is reduced with irradiation [20].

The application of carbon X-ray absorption near edge structure (XANES) in environmental studies includes work on coal, aquatic humic and fulvic acids [21,22,15,23] and reactivity of natural organic matter (NOM) inorganic-mineral associates [16,15]. The objective of our investigation is to compare XANES spectra measured on the carbon K-edge, potassium L-edge, calcium L-edge, oxygen K-edge and iron L-edge with synchrotron based mid-infrared microspectroscopy in order to determine:

(a) the nanoscopic spatial distribution and functional group composition of organic matter in clay-rich low-carbon sedimentary rocks, namely, the Callovo-Oxfordian argillite considered as possible host rock formations for storage of high-level nuclear waste (HLW);
(b) to localize possible sources for hydrophilic bitumen like material (humic and/or fulvic acids) released in this undisturbed sediments, and;
(c) to investigate the radiation damage sensitivity of different natural organic-mineral associates in the dry hard rock.

2. Materials and methods

2.1. Sample origin

The Callovo-Oxfordian argillite sample investigated in this study originates from core material of the exploration bore hole EST 104 (447 m depth) located near Bure (eastern Paris Basin, departments Meuse and Haute-Marne) [16,15]. The argillite sample contains 40–45% clay minerals, ~50% calcite and quartz. Detailed mineralogical studies on the composition of the clay fraction <2 μm revealed for this sample a higher amounts of 2:1 layer silicates (13–20% smectite) indicating an mixed terrestrial/marine deposition environment [16,24,25]. The total organic carbon (TOC) concentration is between 0.4 and 1.4 wt.% in the Callovo-Oxfordian argillite [26]. The maximum burial temperature of the Callovo-Oxfordian argillite probably never exceeded 40 °C as indicated by biomarker and fluid inclusion analysis [27,28].

2.2. Sample preparation

To prevent cross-contamination with organic embedding materials (e.g., epoxy-resin) part of the untreated dry rock sample was embedded in sulfur and thin-sectioned (ultra-microtomed) (MVA, Inc., Norcross, GA) to a thickness of 100 nm and transferred to low-carbon TEM Formvar grids for spectroscopic investigations.

A rock material aliquot was furthermore used to isolate the soluble organic fraction, namely, humic (HA) and fulvic (FA) acids. HA/FA isolation was obtained by a modified International Humic Substance Society (IHSS) isolation procedure [29,30]. For details on the extraction procedure it is referred to [11]. 5.2 and 1.3% of the total organic carbon (TOC) were isolated as HA and FA, respectively. The major part of the natural organic matter inventory in the Callovo-Oxfordian argillite is high-molecular weight, hydrophobic organic matter called kerogen. The kerogen was isolated using the procedure described in detail in [31].

2.3. X-ray absorption near edge structure (XANES) spectromicroscopy

Scanning transition X-ray microscope (STXM) measurements were performed at the National Synchrotron Light Source (NSLS), Brookhaven National Laboratories (BNL) in New York, undulator beamlines X1A1 (elements C, K and Ca) and X1A2 (elements O and Fe), operated by the State University of New York at Stony Brook [32]. The principle of this method is described in detail elsewhere [32,33]. Carbon K-edge, potassium L-edge and oxygen K-edge spectra were recorded in constant helium atmosphere using an undulator gap of 36.8 mm, whereas for iron L-edge and calcium L-edge measurements an undulator gap of 41.7 mm was set. The Fresnel zone plate utilized for C-, K- and Ca-edge measurements had a diameter (a) of 160 μm and a outermost zone width (δ) of 45 nm, whereas for O- and Fe-edge measurements a zone plate with $a = 80$ μm and $\delta = 30$ nm was used. Energy calibration of the spherical grating monochromators was performed by using the photon energy of the CO_2 gas adsorption band at 290.74 eV (X1A1) and the O_2 gas adsorption band at 530.82 eV (X1A2), respectively [34,35]. XANES spectra were recorded using the image stack option [36].

STXM measurements yield information on the optical density (OD) or the product of sample thickness d, the sample density ρ and the mass absorption coefficient $\mu(E)$, which is related to the quotient of the incident flux on the sample $I_0(E)$ and the flux detected behind the sample $I(E)$ via:

$$\mathrm{OD} = -\ln\left[\frac{I(E)}{I_0(E)}\right] = \mu(E)\rho d \quad (1)$$

Image stacks are acquired by taking images at different energy levels across the absorption edge, and aligning them using cross-correlation. After stack alignment the XANES spectra can be extracted. Image regions free of sample gave the $I_0(E)$ information. For STXM analysis the isolated humic/fulvic acids as well as the kerogen isolate were prepared by drying a 0.5–1 μL droplet on a 100 nm thick Si_3N_4 window.

For comparison, all XANES spectra were baseline corrected and normalized to 1 at 295 eV prior to peak fitting. Each normalized carbon XANES spectrum was then further resolved into its individual arctangent [37] and Gaussian curve components, using the nonlinear least-squares fitting routine SOLVER of Microsoft Excel. One ionization threshold (IP) was set for C(1s) XANES spectrum deconvolution (arctangent function at 290.4 eV for aromatic/aliphatic carbon [38,39]) with full width at half maximum (FWHM) of 0.5 eV to generate the continuum spectrum up to 300 eV. The parameter choice overemphasizes contributions to the continuum absorption at low energies and represents a conservative choice. FWHM of Gaussian peaks was loosely constraint between 0 and 0.5 eV and 7 Gaussian functions representing the main 1s–π* or Rydberg/mixed valence transitions (284.3, 285.1, 286.4, 287.4, 288.4, 289.4 and 290.2 eV) were used. The Gaussian peak at 290.2 eV was additionally implemented to account for the C1s(C=O)→$\pi^*_{C=O}$-transition of inorganic carbonate. Following the work of Cody and coworkers [21,40] the energy of inner-shell transition (1s–π*) is accompanied by a second, higher energy transition (1s–2π*) occurring approximately 4 eV above the energy of the 1s–π*-transition with nearly one-quarter of intensity. In order to achieve semi-

quantitative information on spectra de-convolution this transition has been implemented. One σ*-transition (~293 eV) was simulated by simplified Gaussian shape function with a FWHM of <2 eV. The energy position for the aliphatic carbon and the inorganic carbonate were fixed at 287.4 and 290.2 eV, respectively. The energy range for the red shift region due to heteroatom substitution/aromatic ring destabilization or benzoquinone functional groups was limited to ≤284.4 eV, whereas all other Gaussian peak positions were allowed to change freely. Further details on the de-convolution procedure for semi-quantitative analysis of functional group content and the correlation with quantitative analysis by ^{13}C NMR can be found elsewhere [41,23].

The analytical approach used in this study to characterize the natural organic matter–mineral association and to localize spectral similarities between the organic matter present in the untreated rock and the extracted HA/FA and kerogen-type organics was the following:

(a) For characterization of mineral bound organic matter in the whole rock sample the approach described in detail in [42] finding groupings of spectromicroscopic data without prior knowledge of the spectra was used. The data analysis was performed in a two step process: First, spectromicroscopic data was orthogonalized and analytical noise eliminated through principal component analysis (PCA) [43]. Secondly, cluster analysis [44] was performed to classify pixels according to their spectra similarity and recovering gradations of thickness.
(b) Target spectra analysis was performed by using a linear combination of the principal components found under (a) fitting the carbon K-edge target spectra of isolated humic/fulvic acids and kerogen. This method allows identifying regions (maps) of spectral similarity between the untreated whole rock sample and the isolated organic extracts.

2.3.1. Dose calculations and spectra interpretation

Dose scans: A series of X-ray microscopy images were acquired of the thin sectioned argillite rock sample in order to expose the sample to a known radiation dose. Images were taken at 525 eV scanning the sample with a step size of 15 nm and a dwell time of 100 ms/pixel at room temperature giving an average dose per scan of approximately 150 MGy.

Spectral scans: Oxygen K-edge spectral scans in-between the dose scans were also performed by the imaging mode under coarse resolution of 0.1 μm step size and short dwell time of 1 ms to ensure low-dose spectroscopy. The average radiation exposure during a spectral stack at the oxygen K-edge was approximately 7 MGy. A segmented silicon detector with 90% efficiency at 525 eV recorded the transmitted flux at each energy step [45,46].

After a sequence of 12 dose and spectral scans a final larger field image was taken on the oxygen K-edge to ensure that the specimen remained centred on the X-ray beam axis. After dosage on the oxygen K-edge the thin section (microtome) was mounted on the sample holder of the outboard STXM (X1A1) to retrieve additional information on radiation induced changes at the carbon K-edge.

Dose calculations were performed following the approach described in [47]. The dose was calculated using the following formula:

$$\text{Dose} = 1.602 \times 10^{-4} \left(\frac{ENt\mu}{\rho A \eta} \right) \quad (2)$$

where E is the photon energy in eV, N is the number of photons per second absorbed by the sample, measured in kHz, η is the efficiency of the detector, t is the exposure time in ms, ρ is the density in g cm^{-3} (assumed in this study to be 1.0 g cm^{-3} for carbon), A is the radiated area in μm^2, d is the thickness in μm and μ is the inverse absorption length in μm^{-1}. The absorption length μ is expressed therein as:

$$\frac{1}{\mu} = 2 r_e \lambda \left(\frac{N_A}{M} \right) \rho f_2 \quad (3)$$

where $r_e = 2.812 \times 10^{-15}$ m, N_A is the Avogadro number, M is the atomic weight and f_2 is the imaginary part of the complex atomic scattering factor, which was retrieved from tabulated values [48].

The C=O functional group peak intensity changes (i.e., aldehyde, ester, ketone, amide and/or carboxylic acids) due to the O1s(C=O) → π*$_{C=O}$-transition in the oxygen XANES around 530.8–532.8 eV [39,49–51] was used to quantify the degree of damage. The height of this peak was used to quantify the C=O bond density loss. To determine the overall oxygen and carbon mass loss, each spectrum was fitted with the average optical density (OD) at the low-energy (525–528 eV or 280–283 eV) and at the high-energy end (550–551 eV or 294–296 eV) of the spectrum. The ratio of the two average values was used to determine the mass loss as a function of dose using differential absorption analysis [52].

2.4. Synchrotron FT-IR microspectroscopy

Infrared measurements were performed at the U10B beamline (National Synchrotron Light Source) using a Spectra-Tech Continuum IR microscope coupled to a Nicolet Magna 860 FTIR. The microscope utilizes a dual remote masking aperture and matching 32x Schwartzchild objectives [53]. Area mapping was performed using the dual remote masking aperture to define the sample area and spectra were collected with 8 μm × 8 μm aperture by averaging 1024 scans in the wavenumber range 650–4000 cm^{-1} per point in transmission mode at 4 cm^{-1} resolution using Atlμs software (Thermo Nicolet Instruments). Background information is collected through the blank Si_3N_4 window.

3. Results and discussion

3.1. PCA and cluster analysis of XANES spectromicroscopic data

The combination of the carbon, calcium, potassium, oxygen and iron edge spectra in this study gives the possibility to differentiate under sub-micrometer resolution between organic association to carbonate minerals, illitic clays and smectitic clays in the heterogeneous mineral assemblage of a whole rock thin section (microtome).

The smectite-rich region was identified in the upper sector (Fig. 1B, cluster 1) because of the absence of absorption bands at the potassium $L_{2,3}$-edge and at the energy of 290.2 eV (π*-transitions for carbonate) and a detectable absorption at the calcium $L_{2,3}$-edge representing the exchangeable interlayer cations (Fig. 1C). The smectite region is strongly enriched in organic material as indicated by the highest C(1s) XANES edge jump. In the lower part of the thin section two regions of general lower overall organic carbon content can be differentiated. One region (Fig. 1B, cluster 2) shows a significant absorption at the potassium $L_{2,3}$-edge, a considerable calcium K-edge absorption and a small iron $L_{2,3}$-edge absorption indicative for illitic clays or smectite/illite mixed layer minerals (MLM). This region shows significant different carbon edge spectra with lower absorption in the aromatic carbon region and higher aliphaticity (Table 1). The region/cluster 3 (Fig. 1 B, C) identified displays very strong calcium K-edge absorption, and a strong absorption band at 290.2 eV in the carbon K-edge spectra indicative for carbonate. Taking the splitting of the main peaks labeled as a_1 and a_2 (L_3-edge) and b_1 and b_2 (L_2-edge) of Fig. 1C the structural environment surrounding the Ca atoms can be determined. The ΔL_3

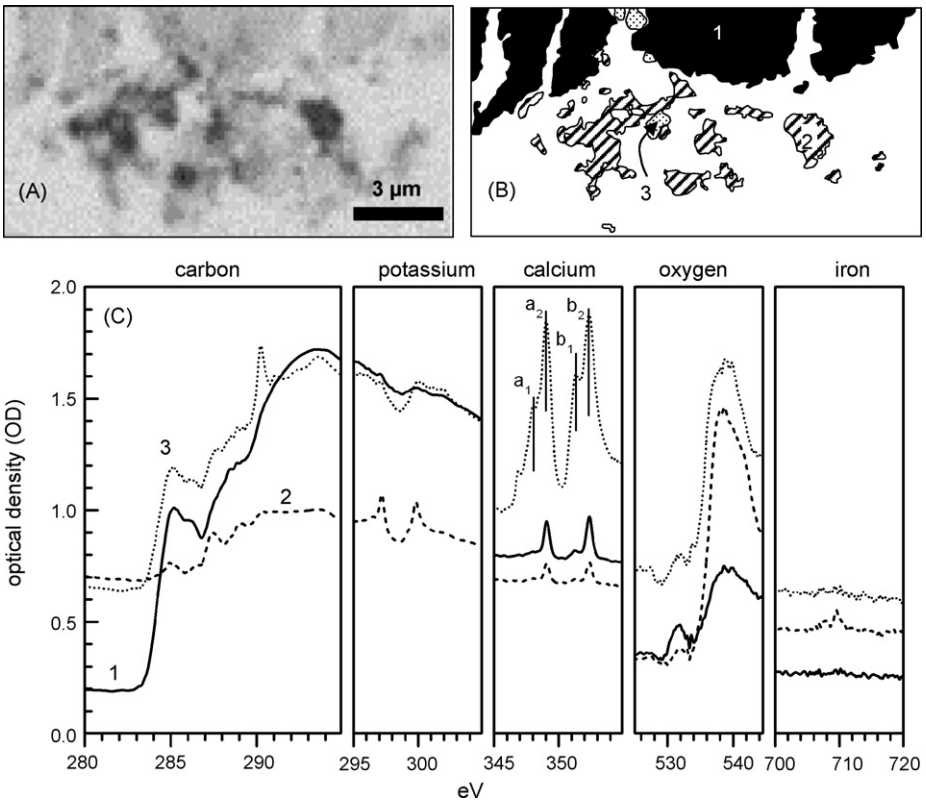

Fig. 1. STXM analysis of Callovo-Oxfordian argillite rock thin section (microtome); sample 447 depth. (A) Absorption image taken at 280 eV below the carbon K-edge. (B) Distribution of the three cluster regions identified using the first eight significant principle components out of the PCA analysis (1: black area; 2: diagonal line hatch; 3: dotted area). Cluster analysis was performed over the energy range 280–740 eV with the following set-up: 4 clusters seeking procedure, eigenimage scaling factor: 0.2, first principal component removed, Euclidean distance measurement. (C) Respective combined carbon, potassium, calcium, oxygen and iron absorption spectra of the clusters identified (cluster 1: solid line; cluster 2: dashed line, cluster 3: dotted line). Additionally the main peaks of the Ca $L_{2,3}$-edge are labeled.

(a_2–a_1) and ΔL_2 (b_2–b_1) parameters of 1.2 and 1.2 eV, respectively, are in very good agreement with published values of 1.3 eV (ΔL_3) and 1.2 eV (ΔL_2) for $CaCO_3$ [55]. From this spectroscopic results we can deduce that the organic matter found in cluster 3 is associated to carbonate phases, most probably a mixed (Fe, Ca)-carbonate or nano-crystalline intergrowth of pure siderite and calcite end members, not resolved by the resolution of STXM (<50 nm).

The carbon edge of the smectite-rich region (cluster 1) and the carbonate rich region (cluster 3) are surprisingly very similar in the overall features with the sole difference of a increased absorption at the C(1s) π*-transition of 290.2 eV for carbonate and the general lower organic association with carbonate as indicated by the edge jump.

Overall, these data clearly demonstrate a higher natural organic matter concentration with smectite type clay minerals. ^{14}C activity measurements in a recent Savanna system have demonstrated that clay mineralogy has a strong influence on the organic matter preservation, with smectite having significantly lower organic matter turn over and higher mean residence time [56]. Therefore, the mineralogy dependent organic carbon concentration and functionality differences observed in this ancient Callovo-Oxfordian sediments (sample 447 m) leads to the conclusion, that the organic matter overprint by digenesis has not eliminated all sedimentary signatures. The de-convolution of the average spectra (Table 1) extracted from the smectite-rich region revealed a significantly higher portion of aromatic carbon (41%) and a lower aliphatic carbon content

Table 1
Semi-quantitative analysis of the average carbon K-edge by spectra de-convolution in the energy range 280–295 eV

Sample	Red shift area[a]	C_{arom}	Phenol-type	$C_{aliph.}$	Carboxyl-type	*O*-alkyl-type	Carbonate	$\Sigma(I_{fit}-I_{meas})^2$
HA isolate	4 (284.3)	19 (285.1)	14 (286.2)	15	24 (288.4)	12 (289.5)	11	0.009642
FA isolate	3 (284.3)	21 (285.1)	13 (286.2)	17	28 (288.4)	9 (289.5)	9	0.008582
Kerogen isolate	4 (284.3)	19 (285.2)	12 (286.3)	18	24 (288.4)	15 (289.6)	8	0.057850
Rock microtome								
Smectite region	5 (284.3)	19 (285.1)	17 (286.2)	17	17 (288.4)	13 (289.4)	12	0.003910
Illite/MLM region	0 (284.3)	8 (285.1)	3 (286.4)	22	17 (288.3)	29 (289.2)	21	0.031310
Carbonate region	5 (284.3)	17 (285.1)	15 (286.2)	17	20 (288.4)	11 (289.4)	15	0.016782
After radiation								
Smectite region	4 (284.3)	20 (285.1)	19 (286.3)	15	17 (288.3)	13 (289.4)	12	0.008230
Illite/MLM region	0 (284.2)	20 (285.1)	8 (286.3)	16	18 (288.2)	21 (289.3)	16	0.017620

Values given are proportion in % of the area sum of the seven π* and the C_{aliph} mixed valence state/Rydberg transition simulated by Gaussian peaks. The energy positions are given in brackets for each Gaussian peak in eV. The energy position for aliphatic carbon $C_{aliph.}$ and inorganic carbonate were fixed at 287.4 and 290.2 eV, respectively.

[a] Red shift due to hetero-atom substitution/aromatic ring destabilization or benzoquinone type functional groups.

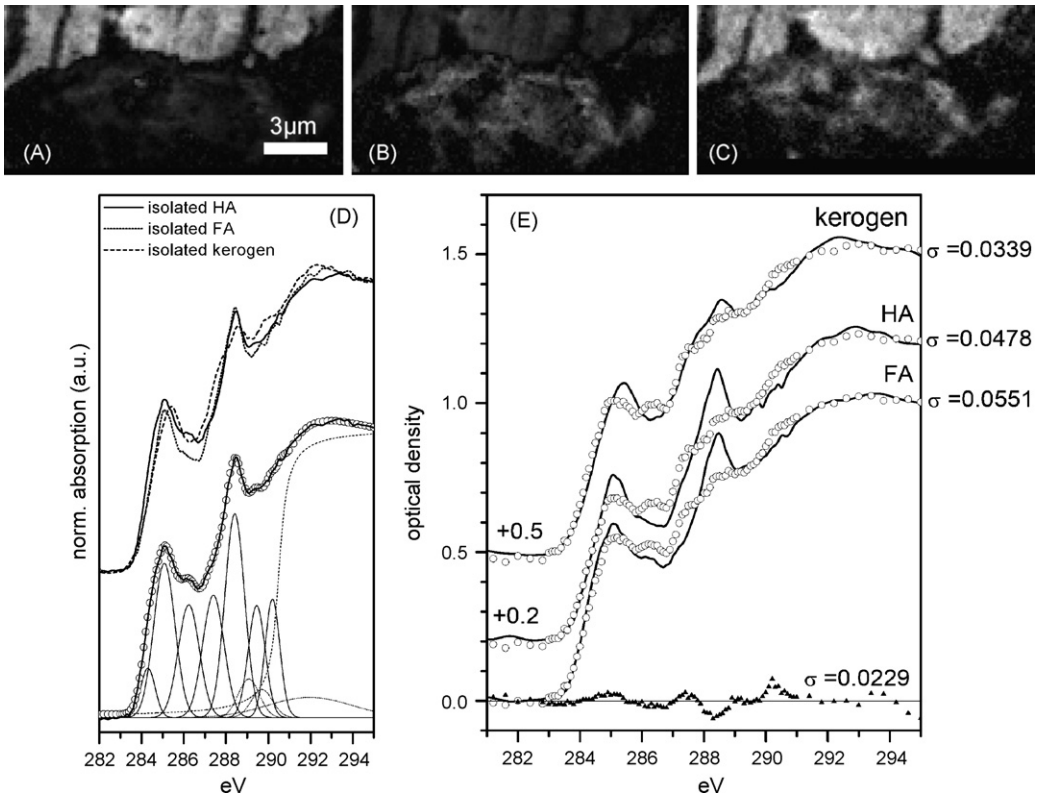

Fig. 2. Target spectra analysis of the STXM data. In Figures A, B, C the generated maps from target spectra fits using isolated humic acid (HA), isolated fulvic acid (FA) and isolated kerogen, respectively, are shown. Light grey values indicate good correlation. Figure D shows the normalized spectra of the isolated HA, FA and kerogen and the applied de-convolution procedure exemplarily for isolated HA. Figure E gives the fits of isolated HA, FA and kerogen target spectra using the first four significant principle components $S_{abstract}$ out of the PCA analysis (open circles) and the original isolated HA, FA and kerogen target spectra (solid lines).

(17%) compared to the illite/mixed layer mineral (MLM) region with 11% aromatic carbon and 22% aliphatic carbon, respectively. No particulate or amorphous organic matter (AOM) without mineral association could be observed in sample 447 under the given resolution of the STXM microscope.

3.2. Target spectra analysis to determine possible HA/FA and kerogen source

To estimate the source of soluble organic matter (i.e., isolated humic and fulvic acid) and hydrophobic kerogen in the whole rock sample, the respective spectra shown in Fig. 2D are used as target spectra to fit the first four principle components out of the PCA analysis [42].

De-convolution of the isolated FA (Table 1) showed a higher aliphaticity of 17% compared to 15% for the isolated HA. The determined carbonate content in the isolated HA and FA is not an impurity of the sample, but a result of the fitting procedure in order to compare these spectra with the thin section (microtome) derived XANES spectra.

The maps of the raw target spectra (not shown separately) and the fitted target spectra show in general a good correlation with light gray regions indicating high concentrations of spectra constituents and dark areas being a sign of depleted regions of target spectra. From the fitted target spectra maps (Fig. 2A, B, C) and the results of the cluster analysis (Fig. 1) the smectite-rich region can be identified as probable source of isolated HA, whereas the isolated FA shows more similarities to the illite/MLM region of the thin section (microtome). The kerogen spectrum shows good correlations to both regions. However, detailed comparison of target spectra with the fitting results show a general trend of increasing conformity in the order FA, HA and kerogen (σ = 0.0339–0.0551) and systematic variations. The isolated FA, HA and kerogen have a significantly higher amount of carboxylic groups (288.6 eV) as well as C_{arom} = C_{arom} or C_{arom}–H (285.2 eV), whereas a lower absorption intensity at 287.4 eV (C_{aliph}) and 286.6 eV (phenol type or keto, enol groups), respectively, is observed.

Released hydrophilic HA or FA are a minor fraction representing the bituminous part in the overall carbon inventory mostly of kerogen-type. Therefore, it is not surprising that the best correlation can be found using the isolated kerogen as target spectra.

Furthermore the sample is measured in transmission and hydrophilic compounds released from the uppermost ~10 nm of the clay-organic coating diminish in the bulk C(1s) spectra. The decreased 287.4 eV intensity assigned to the mixed valence/Rydberg transition C–H* in the HA/FA target spectra can be explained by a decreased carbon atom number (chain length) in the alkyl pendant group [57]. This observation together with the significantly lower carboxyl type groups (1s–π^*-transition of C=O) indicates a higher polymerization of the kerogen-type organic matter compared to the organic surface layer (HA/FA origin). Similar observations with aromatic, carbohydrate and carboxylic acid-like structures in the surface layer and increased aliphatic content in the bulk organic matter were found in studies of recent wetland soil in Saskatchewan [58].

3.3. Synchrotron based FT-IR microspectroscopy

The infrared spectra of the thin section (microtome) is shown in Fig. 3. A differentiation of the clay mineral assemblage as performed by X-ray diffraction could not be accomplished [24,11]. In the region of Al–OH stretching vibrations of the alumosilicate layers, a broad

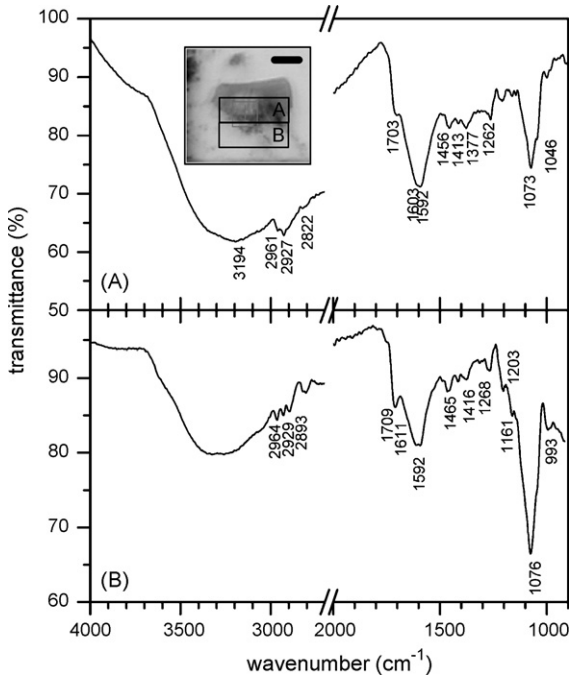

Fig. 3. Synchrotron based infrared microspectroscopy of Callovo-Oxfordian argillite sample 447 m depth. (A) Average spectra extracted from the smectite-rich region, (B) average spectra of the illite/MLM region. Bar length 10 μm.

absorption at 3625 cm^{-1} and two additional signified peaks at 3666 and 3694 cm^{-1} could be identified. This broad hydroxyl absorption is typical for random substitution present in dioctahedral micas and smectites, where the MgAlOH absorption at 3687 cm^{-1} could not be resolved from the Al_2OH absorption at 3620–3630 cm^{-1} [59]. The additional peak at 3666 cm^{-1} can be assigned to a weak OH-stretching feature of trioctrahedral chlorites. Kaolinite group minerals typically showing three sharp high frequency features at 3697, 3669 and 3652 cm^{-1} beside the 3620 cm^{-1} inner hydroxyl group band could not be differentiated, as expected [59]. The band at 1161 cm^{-1} can be assigned to the C–C bond in aliphatics and polymeric substances or to a Si–O–C bond, which might indicate a linkage of some organic macromolecules to the clay Si–O groups [60]. The absorption bands around 1076, 1039, 916 cm^{-1} and the doublet around 800 cm^{-1} can be identified as Si–O or Al–OH vibrations in quartz and/or alumosilicates, whereas the absorption band near 1415 cm^{-1} can be assigned to the asymmetrical stretch of CO_3^{2-} in carbonates [59].

Characteristic bands for organic components include OH groups of phenols, alcohols and carboxylic OH near 3430–3383 cm^{-1}, aromatic CH groups by a shoulder at 3073 cm^{-1}, aliphatic CH_2 and CH_3 bands at 2929, 2870, 1450 and 1375 cm^{-1}, a carboxylic band of ketones, acids or esters at 1715 and 1261 cm^{-1}, peptide amide I and amide II bands at 1650 and 1540 cm^{-1} and the band at 1630 cm^{-1} for mostly aromatic C=C [4,60]. The above-mentioned aliphatic CH_2 and CH_3 bands can be furthermore separated into a exclusively CH_3 absorption at 1375 cm^{-1} and a mixed linear CH_3 and cyclic CH_2 vibration at 1455 cm^{-1}[4]. To estimate the length, the degree of aliphatics and side-chain branching the technique of CH_2/CH_3 (2915–2940 cm^{-1}/2950–2975 cm^{-1}) intensity ratio measurement outlined in detail in [61] was applied. Furthermore data analysis was performed by an A-factor (3000–2800 cm^{-1}/3000–2800 cm^{-1} + 1650–1520 cm^{-1}), C-factor (1800–1650 cm^{-1}/1800–1650 cm^{-1} + 1650–1520 cm^{-1}) calculation, which produces similar results than the classical H/C versus O/C van Krevelen plot (not shown) [62]. The smectite-rich region defined as HA source plots in the region of type III kerogen or terrestrial derived organic material, whereas the illite/MLM region shows higher A-factor (H/C ratio) and C-factor (O/C ratio) values and falls in the region of type II kerogen typical for a marine influenced sedimentation environment. These results are compatible with the general observation of higher aliphaticity in FA compared to HA.

A clear indication of an increased carboxyl group content by a significantly higher absorption at 1709 cm^{-1} in the illite–MLM region can be detected. However, compared to infrared spectra of isolated natural humic or fulvic acids [60,63] or humic-like substances generated in the presence of clays [64] this C=O band intensity of all clay associated organics is significantly reduced indicating a loss of oxygen-containing functional groups as already shown by XANES analysis. A second difference between region A and B (Fig. 3) is the band at 1161 cm^{-1}, which can be identified in the illite rich region B, but cannot be resolved in the smectite-rich region A. Taken into account the C(1s) XANES target spectra analysis derived information of smectite as the potential HA source and the higher HA extraction yield compared to FA [11] of these sediments, a possible explanation of the higher HA mobilization can be the missing Si–O–C linkage of humic macromolecules. Changes in organic functionality due to radiation damage (see below) could not be followed by FT-IR due to the small area irradiated (3 μm × 3 μm) compared to the resolution of the microscope (8 μm aperture in our studies).

3.4. Radiation sensitivity of Callovo-Oxfordian argillite

The radiation damage results are discussed with respect to the above identified smectite and illite–MLM region and associated organic functionality found by PCA and cluster analysis. Both, in the smectite and the illite–MLM dominated region an increase in the optical density below the carbon K-edge after irradiation could be observed (Fig. 4). This radiation induced gain of material from photodeposition observed in images below the C K-edge results in an overall pre-edge optical density increase of 0.05. Assuming hydrocarbon deposition with a structural formula of C_nH_2 for saturated hydrocarbons containing one ring or unsaturated non-cyclic hydrocarbons the total carbon mass loss by radiation damage documented below could be underestimated by roughly 20%.

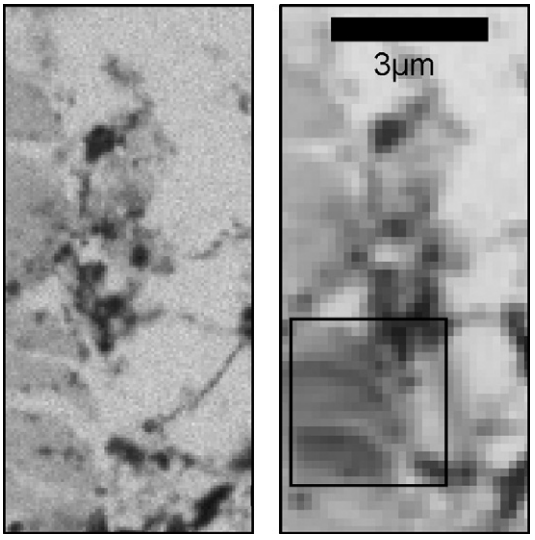

Fig. 4. STXM images taken below the carbon K-edge at 280 eV before radiation (left) and after radiation exposure to 1.7 GGy showing the increase in optical density by darker grey values.

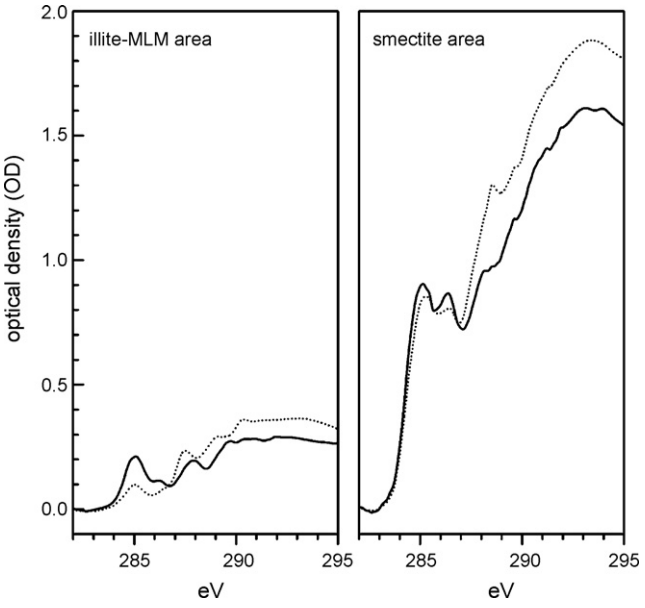

Fig. 5. C(1s) spectra of the illite–MLM area and the smectite clay mineral dominated area before radiation (dotted line) and functional group changes after 1.7 GGy irradiation. Carbon edge mass loss of illite–MLM region is 18% and of smectite-rich area 13%.

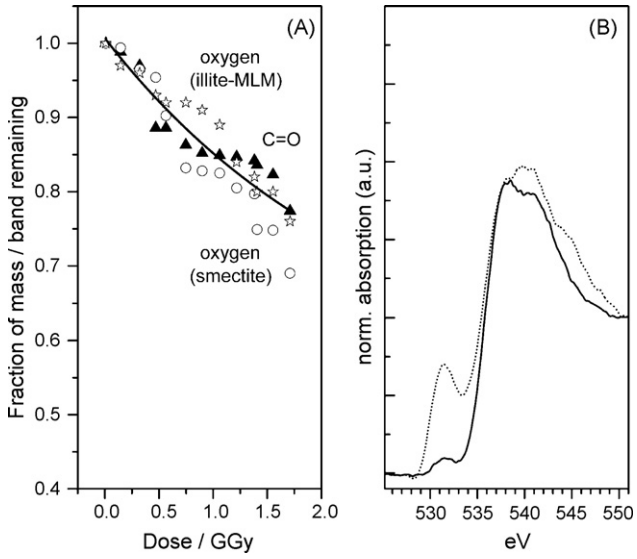

Fig. 6. (A) Fraction of oxygen mass/C=O band remaining after indicated dose (illite–MLM region oxygen mass loss (open stars), smectite region oxygen mass loss (open circles), smectite C=O band intensity loss (filled triangles)). The solid line represents the exponential fit for critical dose determination. (B) Oxygen K-edge spectra before dose scans of smectite region (dotted line) and illite–MLM region (solid line).

However, normalizing the spectra to the pre-edge, the edge jump clearly shows a carbon mass loss on both the carbon and oxygen K-edge after applying a dose of 1.7 GGy (not shown as figure). The total carbon mass loss is in the range of 13% in the smectite-rich area and in a comparable range of ~18% in the of illite–MLM region. The qualitative and semi-quantitative spectroscopic observation on the carbon functionality (Fig. 5, Table 1) show a clear increase in aromatic structures (Σ(benzoquinone + C_{arom} = C_{arom} + phenol-type) especially in the initially lower aromatic illite–MLM associated organics from 11 to 28%, whereas the more aromatic smectite associated organics are less affected. Furthermore, the aliphatic carbon decreased in both regions (Table 1). Comparable results were found, for example, in studies on natural radiation induced alteration of bitumen in uranium deposits from Pribram (Czech Republic), where a depletion of aliphatic CH_2 and CH_3 groups and a higher aromaticity correlated with the amount of bitumen associated uranium [65]. This results suggests a combination of the formation of C=C bond due to crosslinking via polymerization and mass loss due to bond breaking (scissioning) in the main chain or in side groups of the organic macromolecule upon irradiation.

Detailed oxygen mass loss analysis were possible for both clay regions of the thin section (microtome), whereas the damage at the C1s(C=O) $\rightarrow \pi^*_{C=O}$-transition could not by quantified for the illite–MLM region, since the peak height could not be determined with high certainty. As shown in Fig. 6A the radiation damage in the smectite and illite–MLM associated organic matter is comparable with 20–30% mass loss after 1.7 GGy irradiation. Assuming a sum formula for hydrophilic organic matter (bitumen or humic and fulvic acids) of $CO_{0.5}H$ the oxygen edge mass loss would correspond to a carbon mass loss of approximately 10–15%, which is in quite good agreement with the C(1s) XANES observations. Using the approach of [66] the mass loss or loss in optical density for the C1s(C=O) $\rightarrow \pi^*_{C=O}$-transition can be quantified by the following exponential expression:

$$OD = OD_\infty + C \exp\left(\frac{d}{d_c}\right) \quad (4)$$

where OD_∞ is the extrapolated optical density or band density after infinite radiation dose, C is a constant, d is the radiation dose and d_c is the critical radiation dose. OD_∞ is fitted by a first-order kinetics process given in Eq. (4) and determines the absorbance remaining after the radiation damage process saturates. At the critical radiation dose $1/e$ or 63% of the total attenuation of the specific spectroscopic feature (or mass thickness) has occurred. Due to the very similar radiation damage behavior on the oxygen edge of both clay regions, average values were calculated. A critical dose d_c of 2.5 GGy and a saturated optical density after infinite radiation of 54% of the initial OD was calculated with a quadric Pearson correlation coefficient (r^2) of 0.88671 under room temperature.

Although this results indicate a rather low sensitivity to high radiation doses of the Callovo-Oxfordian organic matter, all analysis were performed under helium atmosphere. Polymer studies have already shown that helium atmosphere compared to air can reduce the damage rate by a factor of ~100 [66]. Further studies under more relevant conditions (e.g., presence of air or porewater) are underway to draw final conclusions on radiation induced changes of kerogen/bitumen present in potential high-level nuclear waste host rock formation.

4. Conclusions

Combination of carbon, potassium, calcium, oxygen and iron XANES spectra using PCA and cluster as well as target spectra analysis revealed in the Callovo-Oxfordian argillite a mineral dependent organic matter functionality. Furthermore this method is capable to identify spectral similarities of isolated humic and fulvic acids in the undisturbed rock sample under nanoscopic spatial resolution. Using synchrotron based FT-IR microspectroscopy, with its high sensitivity to aliphatic carbon, it was also possible to retrieve additional information on the deposition environment. These results demonstrate that even in approx. 160 Ma old geological formations, part of the organic inventory keeps the structure/functionality of hydrophilic HA/FA. After radiation of 1.7 GGy under helium atmosphere the same area was investigated for radiation damage. Radiation damage in the smectite and illite–MLM associated organic matter is comparably low with 20–30% total oxygen mass loss and 13–18% total carbon mass loss. This result indicates a rather low sensitivity of the Callovo-Oxfordian organic matter indepen-

dent of clay type to high radiation doses under helium atmosphere. A critical dose d_c of 2.5 GGy and an optical density (OD) after infinite radiation of 54% of the initial OD was calculated under room temperature conditions. C(1s) XANES show a clear increase in C=C bonds more pronounced in the initially lower aromatic illite–MLM associated organics. These results suggest a combination of the formation of C=C bond due to crosslinking via polymerization and mass loss due to bond breaking (scissioning) to appear in parallel on the organic macromolecules upon irradiation.

Acknowledgements

This work was financed through the 'FUNMIG project' (EC: FUNMIGNUWASTE-2004-3.2.1.1-1) and the EURATOM Intra-European fellowship 'COMACK' (FI6W-CT-2006-036493). We are grateful for beamtime allotment by BNL/NSLS. The National Synchrotron Light Source is supported by the U.S. Department of Energy, Division of Materials Sciences and Division of Chemical Sciences, under Contract No. DE-AC02-98CH10886. Spectromicroscopic data were collected using the X1-A1 STXM developed by the group of Janos Kirz and Chris Jacobsen at SUNY Stony Brook, with support from the Office of Biological and Environmental Research, U.S. DoE under contract DE-FG02-89ER60858, and from the NSF under grant DBI-9605045. The zone plates were developed by Steve Spector and Chris Jacobsen of Stony Brook and Don Tennant of Lucent technologies Bell Labs with support from the NSF under grant ECS-9510499.

References

[1] J.I. Hedges, F.S. Hu, A.H. Devol, H.E. Hartnett, E. Tsamakis, R.G. Keil, Am. J. Sci. 299 (1999) 529.
[2] J.I. Hedges, R.G. Keil, Mar. Chem. 49 (1995) 81.
[3] J.I. Hedges, R.G. Keil, Mar. Chem. 49 (1995) 137.
[4] B.P. Tissot, D.H. Welte, Petroleum Formation and Occurrence, Springer, Hamburg, 1984.
[5] E.W. Tegelaar, J.W. Deleeuw, S. Derenne, C. Largeau, Geochim. Cosmochim. Acta 53 (1989) 3103.
[6] J.S. Sinninghe Damste, W.I.C. Rijpstra, A.C. Kock-van Dalen, J.W. De Leeuw, P.A. Schenck, Geochim. Cosmochim. Acta 53 (1989) 1343.
[7] S.M. Henrichs, Mar. Chem. 49 (1995) 127.
[8] F. Khalili, Fuel 69 (1990) 151.
[9] L.R. Krumholz, S.H. Harris, J.M. Suflita, Geomicrobiol. J. 19 (2002) 593.
[10] F. Claret, T. Schäfer, A. Bauer, G. Buckau, Sci. Total Environ. 317 (2003) 189.
[11] F. Claret, T. Schäfer, T. Rabung, M. Wolf, A. Bauer, G. Buckau, Appl. Geochem. 20 (2005) 1158.
[12] R. Artinger, W. Schuessler, T. Schäfer, J.I. Kim, Environ. Sci. Technol. 36 (2002) 4358.
[13] H. Geckeis, T. Schäfer, W. Hauser, T. Rabung, T. Missana, C. Degueldre, A. Möri, J. Eikenberg, T. Fierz, W.R. Alexander, Radiochim. Acta 92 (2004) 765.
[14] T. Schäfer, H. Geckeis, M. Bouby, T. Fanghänel, Radiochim. Acta 92 (2004) 731.
[15] T. Schäfer, F. Claret, A. Bauer, L. Griffault, E. Ferrage, B. Lanson, J. Phys. IV 104 (2003) 413.
[16] F. Claret, A. Bauer, T. Schäfer, L. Griffault, B. Lanson, Clay Clay Miner. 50 (2002) 633.
[17] M. Plötze, G. Kahr, R.H. Stengele, Appl. Clay Sci. 23 (2003) 195.
[18] W.J. Weber, R.C. Ewing, C.A. Angell, G.W. Arnold, A.N. Cormack, J.M. Delaye, D.L. Griscom, L.W. Hobbs, A. Navrotsky, D.L. Price, A.M. Stoneham, W.C. Weinberg, J. Mater. Res. 12 (1997) 1946.
[19] B.X. Gu, L.M. Wang, L.D. Minc, R.C. Ewing, J. Nucl. Mater. 297 (2001) 345.
[20] M.D. Lewan, G.F. Ulmishek, W. Harrison, F. Schreiner, Geochim. Cosmochim. Acta 55 (1991) 1051.
[21] G.D. Cody, R.E. Botto, H. Ade, S. Behal, M. Disko, S. Wirick, Energy Fuels 9 (1995) 525.
[22] M. Plaschke, J. Rothe, T. Schäfer, M.A. Denecke, K. Dardenne, S. Pompe, K.H. Heise, Colloids Surf. A 197 (2002) 245.
[23] T. Schäfer, G. Buckau, R. Artinger, J.I. Kim, S. Geyer, M. Wolf, W.F. Bleam, S. Wirick, C. Jacobsen, Org. Geochem. 36 (2005) 567.
[24] F. Claret, B.A. Sakharov, V.A. Drits, B. Velde, A. Meunier, L. Griffault, B. Lanson, Clay Clay Miner. 52 (2004) 515.
[25] P. Landais, M. Elie, Utilisation de la géochimie organique pour la détermination du paléoenvironnement et de la paléothermicité dans le Callovo-Oxfordien du site de l'Est de la france. Etude de lïEst du bassin de Paris, Edition EDP Sciences, 1999, pp. 35.
[26] I. Deniau, I. Devol-Brown, S. Derenne, F. Behar, C. Largeau, Sci. Total Environ. 389 (2008) 475.
[27] P. Pellenard, J.F. Deconinck, D. Marchand, J. Thierry, D. Fortwengler, G. Vigneron, C. R. Acad. Sci. Paris, Sciences de la terre et des planetes 328 (1999) 807.
[28] M. Elie, P. Faure, R. Michels, P. Landais, L. Griffault, Energy Fuels 14 (2000) 854.
[29] G. Buckau, Komplexierung von Americium (III) mit Huminstoffen in natürlichen Grundwässern. Ph.D. Thesis, Freie Universität Berlin, Berlin.
[30] R.S. Swift, in: D.L. Sparks (Ed.), Methods of Soil Analysis Part 3: Chemical Methods, SSSA Book Series: 5, Soil Science Society of America, Inc., Madison, WI, 1996, Chapter 35.
[31] M. Vandenbroucke, C. Largeau, Org. Geochem. 38 (2007) 719.
[32] C. Jacobsen, S. Williams, E. Anderson, M.T. Browne, C.J. Buckley, D. Kern, J. Kirz, M. Rivers, X. Zhang, Opt. Commun. 86 (1991) 351.
[33] X. Zhang, H. Ade, C. Jacobsen, J. Kirz, S. Lindaas, S. Williams, S. Wirick, Nucl. Instrum. Meth. A 347 (1994) 431.
[34] A.P. Hitchcock, D.C. Mancini, J. Electron Spectrosc. Relat. Phenom. 67 (1994) 1.
[35] Y. Ma, C.T. Chen, G. Meigs, K. Randall, F. Sette, Phys. Rev. A 44 (1991) 1848.
[36] C.J. Jacobsen, C. Zimba, G. Flynn, S. Wirick, J. Microsc.-Oxford 197 (2000) 173.
[37] J. Stöhr, NEXAFS Spectroscopy. Springer Series in Surface Sciences, 25, Springer, Berlin, 1996.
[38] A.P. Hitchcock, I. Ishii, J. Electron Spectrosc. Relat. Phenom. 42 (1987) 11.
[39] A.P. Hitchcock, S.G. Urquart, E.G. Rightor, J. Phys. Chem. 96 (1992) 8736.
[40] G.D. Cody, R.E. Botto, H. Ade, S. Wirick, Int. J. Coal Geol. 32 (1996) 69.
[41] T. Schäfer, N. Hertkorn, R. Artinger, F. Claret, A. Bauer, J. Phys. IV 104 (2003) 409.
[42] M. Lerotic, C. Jacobsen, T. Schäfer, S. Vogt, Ultramicroscopy 100 (2004) 35.
[43] E. Malinowski, Factor Analysis in Chemistry, John H. Wiley & Sons, New York, 1991.
[44] B. Everett, S. Landau, M. Leese, Cluster Analysis, Arnold Publishers, London, 2001.
[45] M. Feser, C. Jacobsen, P. Rehak, G. DeGeronimo, J. Phys. IV 104 (2003) 529.
[46] M. Feser, T. Beetz, C. Jacobsen, J. Kirz, S. Wirick, A. Stein, T. Schäfer, in: D.A. Tichenor, J.A.J.A. Folta (Eds.), Soft X-ray and EUV Imaging Systems II, Society of Photo-Optical Instrumentation Engineers (SPIE) 4506, Bellingham, Washington, 2001, p. 146.
[47] T. Beetz, C. Jacobsen, J. Synchrot. Radiat. 10 (2003) 280.
[48] B.L. Henke, E.M. Gullikson, J.C. Davis, Atom. Data Nucl. Data Tables 54 (1993) 181.
[49] J.T. Francis, A.P. Hitchcock, J. Phys. Chem. 96 (1992) 6598.
[50] A.P. Hitchcock, C.E. Brion, J. Electron Spectrosc. Relat. Phenom. 19 (1980) 231.
[51] M.B. Robin, I. Ishii, R. McLaren, A.P. Hitchcock, J. Electron Spectrosc. Relat. Phenom. 47 (1988) 53.
[52] A. Engström, Acta Radial. Suppl. 63 (1946) 1.
[53] P. Dumas, L. Miller, Vib. Spectrosc. 32 (2003) 3.
[55] S.J. Naftel, T.K. Sham, Y.M. Yiu, B.W. Yates, J. Synchrot. Radiat. 8 (2001) 255.
[56] E.J.W. Wattel-Koekkoek, P. Buurman, J. van der Plicht, E. Wattel, N. van Breemen, Eur. J. Soil Sci. 54 (2003) 269.
[57] J. Kikuma, B.P. Tonner, J. Electron Spectrosc. Relat. Phenom. 82 (1996) 41.
[58] A. Jokic, J.N. Cutler, E. Ponomarenko, G. van der Kamp, D.W. Anderson, Geochim. Cosmochim. Acta 67 (2003) 2585.
[59] V.C. Farmer (Ed.), The Infrared Spectra of Minerals, vol. 4, Mineralogical Society, London (UK), 1974, p. 539.
[60] A. Naidja, P.M. Huang, D.W. Anderson, C. van Kessel, Appl. Spectrosc. 56 (2002) 318.
[61] P.C. Painter, M. Starsinic, M.M. Coleman, in: J.R. Ferraro, L.J. Basile (Eds.), Fourier Transform Infrared Spectroscopy, vol. 4, Academic Press, New York, 1985, p. 169.
[62] Ganz, Kalkreuth, Fuel 66 (1987) 708.
[63] K. Schmeide, S. Sachs, M. Bubner, T. Reich, K.H. Heise, G. Bernhard, Inorg. Chim. Acta 351 (2003) 133.
[64] M. Bosetto, P. Arfaioli, O.L. Pantani, Clay Min. 37 (2002) 195.
[65] B. Kribek, K. Zak, J. Spangenberg, J. Jehlicka, S. Prokes, J. Kominek, Econ. Geol. 94 (1999) 1093.
[66] T. Coffey, S.G. Urquhart, H. Ade, J. Electron Spectrosc. Relat. Phenom. 122 (2002) 65.